14 March 2022

Understanding and Utilizing Reactive Oxygen Reservoirs in Atomic Layer Deposition of Metal Oxides with Ozone

Joel Schneider[1], Camila de Paula[1], Nathaniel Richey[1], Jon Baker[1], Solomon Oyakhire[1], Stacey Bent[1]

1. Stanford University

Abstract

Contrary to idealized depictions, atomic layer deposition (ALD) reactions do not always take place solely at the gas-solid interface. The iron oxide ALD system was recently shown to grow by a subsurface mechanism in which reactive oxygen is absorbed into the growing film during ozone exposure, forming an effective reservoir of oxygen. This study investigates the fundamental chemical mechanisms behind the oxygen reservoir phenomenon and extends it to other binary and multicomponent oxide ALD systems. NiO ALD is found to exhibit similar saturation behavior and crystallinity trends with ozone as Fe2O3 ALD. Oxygen uptake from ozone into the film is directly detected in situ for both processes, and in vacuo spectroscopy elucidates possible chemical states of the subsurface oxygen reservoirs in each material. In situ process characterization reveals that the reserved oxygen participates in surface combustion reactions capable of activating ALD growth. The oxygen reservoir mechanism is also shown to generalize to other oxide systems, correlating with trends in oxygen mobility, crystallinity, and metal oxidizability. Finally, the reactive oxygen reservoirs are utilized in the deposition of a multicomponent FeAlxOy material, previously unreported by ALD, revealing that the reserved oxygen can activate growth of other processes and possesses the potential to address nucleation challenges in other ALD systems.

Keywords

atomic layer deposition, thin films, ozone, mechanisms, ternary materials

Understanding and Utilizing Reactive Oxygen Reservoirs in Atomic Layer Deposition of Metal Oxides with Ozone

Joel R. Schneider,[1] Camila de Paula,[1] Nathaniel E. Richey,[1] Jon G. Baker,[1] Solomon T. Oyakhire,[1] and Stacey F. Bent[1,*]

[1]*Department of Chemical Engineering, Stanford University, Stanford, California 94305, USA*

**Email: sbent@stanford.edu*

Abstract

Contrary to idealized depictions, atomic layer deposition (ALD) reactions do not always take place solely at the gas-solid interface. The iron oxide ALD system was recently shown to grow by a subsurface mechanism in which reactive oxygen is absorbed into the growing film during ozone exposure, forming an effective reservoir of oxygen. This study investigates the fundamental chemical mechanisms behind the oxygen reservoir phenomenon and extends it to other binary and multicomponent oxide ALD systems. NiO ALD is found to exhibit similar saturation behavior and crystallinity trends with ozone as Fe_2O_3 ALD. Oxygen uptake from ozone into the film is directly detected *in situ* for both processes, and *in vacuo* spectroscopy elucidates possible chemical states of the subsurface oxygen reservoirs in each material. *In situ* process characterization reveals that the reserved oxygen participates in surface combustion reactions capable of activating ALD growth. The oxygen reservoir mechanism is also shown to generalize to other oxide systems, correlating with trends in oxygen mobility, crystallinity, and metal oxidizability. Finally, the reactive oxygen reservoirs are utilized in the deposition of a multicomponent $FeAl_xO_y$ material, previously unreported by ALD, revealing that the reserved

oxygen can activate growth of other processes and possesses the potential to address nucleation challenges in other ALD systems.

Introduction

Thin films have demonstrated great utility in tackling a variety of scientific challenges across a range of applications.[1–8] In many of these contexts, specific material property, chemistry, and nanostructure needs have driven major developments in fabrication,[9–12] with atomic layer deposition (ALD) having particular power to address requirements for precise, complex, and tunable materials.[9,13,14] While many idealized ALD reactions are presumed to take place in a self-limiting manner confined to only the growth surface, numerous deviations exist in real ALD systems, and thus comprehensive and detailed understandings of ALD growth processes are needed for effective implementation, particularly for precisely designed materials.[1,15] Many non-ideal, complex chemistries have been described in ALD,[14,16–20] including a recent report of unexpected behaviors of oxygen species in iron oxide ALD using ozone.[21] In that report, it was found that rather than the self-limiting formation of a sub-monolayer of surface-bound material at each half cycle, greater than a monolayer of reactive oxygen species from ozone was incorporated subsurface into the film, leading to a more complex mechanism of ALD growth. The present work seeks to further elucidate and generalize this mechanism, as well as apply it to new ALD systems.

This study focuses on ALD of iron oxide, the material previously reported to grow by a subsurface oxygen mechanism, as well as nickel oxide and aluminum oxide. Both nickel and aluminum oxides are of great interest in a variety of applications in catalysis and coatings and

have been implemented in a range of ternary ALD materials,[14,22–27] and their contrasting chemistries can aid in illuminating the oxygen reservoir phenomenon. In oxide ALD processes there are many possible co-reactants that can act as a source of elemental oxygen, including water, oxygen, ozone, and oxygen plasma, and each can react through different surface mechanisms.[14,17] ALD of both nickel[28–30] and iron[31–33] oxides has been reported previously using metallocene precursors, and in these processes ozone or plasma is needed as the oxygen source. Because oxidation of the Fe or Ni metal center and elimination of the stable aromatic Cp ligands are both needed, water and oxygen are generally not reactive enough, and a strong oxidant is required for the co-reactant. While aluminum oxide can be deposited via trimethylaluminum with water, processes with ozone have also been reported extensively in the literature.[34,35] With reactive co-reactants such as ozone and plasma, complex gaseous species can form, and many previous studies have focused on understanding the intricate behaviors of such processes.[36,37]

Rather than focusing on gas phase products, this work builds upon the recent report of Fe_2O_3[21] ALD to investigate a unique subsurface mechanism for reactive species that arising from use of the highly reactive ozone. In addition to Fe_2O_3, we study the growth mechanism of NiO ALD to generalize the finding of a subsurface oxygen growth mechanism and investigate the effect of subsurface reactive species on Al_2O_3 ALD in multicomponent processes. *In situ* characterization tools are used to probe the surface reactions during ALD to gain an understanding of the specific reactive species in the oxygen reservoirs and the resulting surface reactions. Through this understanding, further comparisons between NiO and Fe_2O_3 ALD are made and broader trends identified across other oxide ALD processes, including aluminum oxide. Finally, the active oxygen reservoirs can be applied to new processes, and this work extends Fe_2O_3 into ternary $FeAl_xO_y$ ALD, a process yet unreported in the literature, and

investigates the role active oxygen species play in other ALD processes. Because chemical phenomena, such as persisting species, in each constituent binary ALD process can have significant impacts on the behavior and process of the overall multicomponent process,[14] understanding these phenomena can impact a range of ALD systems. In total, this study identifies a new ALD process that grows by the subsurface oxygen reservoir mechanism, elucidates the chemical nature of the reservoir, probes how the reservoir species participate in ALD reactions, and applies and extends the growth phenomenon to a broader range of ALD processes.

Experimental Methods

Synthesis of Thin Films by Atomic Layer Deposition

Thin film depositions were performed in four different custom-built ALD reactors. All reactors' pressures were monitored using convectron gauges, were pumped using rotary vane pumps, and used N_2 (Praxair, 99.998%) as the purge gas. The first reactor, used for synthesis of samples for *ex situ* analysis and for *in situ* ellipsometry (iSE) characterization, was a perpendicular-flow ALD reactor with a 4-inch heated stage and substrate holder. The purge gas flow rate was 20 standard cubic centimeters per minute (SCCM) to yield a working pressure of 550 mTorr. Precursors and purge gas were introduced through a showerhead above the stage, and substrate temperature was controlled by a heater internal to the stage as reported previously.[21,38,39]

The second, third, and fourth reactors—used for *in situ* quadrupole mass spectrometry (QMS), *in situ* quartz crystal microbalance (QCM), and *in vacuo* X-ray photoelectron

spectroscopy (XPS), respectively—were all tubular, cross-flow ALD reactors with 1.3-inch diameter tubular bodies. The purge gas flow rates in the QCM and XPS reactors varied between 4 and 20 SCCM, depending on the reactor, to maintain working pressures of 400-600 mTorr. The nitrogen flow rate in the QMS was kept below 5 SCCM for working pressures around 140 mTorr to reduce the nitrogen signal detected by QMS. Precursors and purge gas were introduced near the upstream door of each chamber. In the QMS and QCM reactors, temperature was controlled in a hot-wall fashion using heating around the exterior of the reactor body, and substrates were placed on a flat sample holder that rested on the bottom of the tubular reactor body. In the QCM reactor, substrate temperature was additionally monitored through a thermocouple inside the QCM sensor head. For the *in vacuo* XPS reactor, the substrate was mounted on a stainless-steel sample holder which clipped onto a 1 x 2 inch stage that was suspended in the center of the tubular body. The substrate temperature was modulated using cartridge heaters contained internally to the stage, and the reactor walls were maintained at a lower temperature using exterior heating around the reactor body.

The organometallic precursors used for depositions were *tert*-butylferrocene [Fe(Cp)(Cp^{t}Bu), TBF, Strem Chemicals, 98%], nickelocene ($NiCp_2$, Strem, 99%), and trimethylaluminum (TMA, Sigma-Aldrich, 97%). Co-reactants used in ALD processes included deionized water for Al_2O_3 and ozone for NiO and Fe_2O_3. Ozone was generated *in operando* with an IN USA AC-2025 generator from oxygen gas (Praxair, 99.6%). In-line ozone concentration was measured in real time using an IN USA Mini-HiCon Bench analyzer, and concentrations were maintained in the 150-220 grams per normal cubic meter range. For all depositions for *ex situ* characterization, substrates were n-doped (100) silicon coupons with native oxide (WRS Materials) and were cleaned in a Novascan PSD Series Digital UV Ozone system for 15 minutes

immediately prior to film deposition. For *in vacuo* XPS depositions, substrates were SiO_2 thermal oxide. The oxide was formed by cleaning Si(001) wafers in a 2% HF in water solution and then oxidizing in atmospheric pressure O_2 for 2 hours at 1050 °C, resulting in an oxide thickness of approximately 130 nm. A thick thermal oxide was used instead of a thin native oxide for XPS measurements to simplify the structure of the Si 2p peak into a single oxide peak, providing a more accurate reference peak for spectral analysis. Prior to deposition, the thermal oxide coupons were cleaned by sequential sonication in acetone, isopropanol, and deionized water followed by a 15 minute cleaning in the UV Ozone system as described above. For *in situ* QMS experiments, depositions were performed on 0.5 g of high surface-area silica gel (Devisil grade 643, Sigma Aldrich) contained in a powder holder with a mesh covering to prevent powder from dispersing inside the chamber. The powder was likewise cleaned in the same UV Ozone system. Depositions for QCM were performed on a Colnatec RC quartz crystal substrate with alloy leads designed for a 20 °C – 250 °C temperature range. During depositions, all substrates were maintained at a temperature of 220 °C; the TBF canister at 80-90 °C; the $NiCp_2$ canister at 75 °C; and the TMA, H_2O, and O_3 all at room temperature. Since $NiCp_2$ is a solid, the line between the precursor canister and the reactor was held at 95 °C to prevent clogs and aid in delivery. In the ALD reactors with interior stage heating—namely the reactors used for *ex situ* characterization and *in vacuo* XPS—the reactor walls were kept below the substrate temperature at 185 °C.

During depositions, the partial pressures of ozone pulses were consistent at 1.1-1.3 Torr, TMA pulses at 300-400 mTorr, and H_2O at 300-400 mTorr, with very little transient behavior in each. Therefore, the total ozone, TMA, and H_2O exposures were quantified by the total pulse time. To prevent the pump pulling vacuum on the ozone generator, ozone exposures of longer

than 10 seconds were divided into multiple separate pulses of 10 seconds each separated by purge times of 30 seconds to allow for the ozone generation and delivery line to repressurize. In contrast, the partial pressure of TBF and $NiCp_2$ delivered to the reactors in a given pulse varied depending upon experimental parameters. To account for this variability, total precursor exposure for these two metalorganics was quantified by calculating the integrated pressure-time area under the pressure pulses for each precursor during the exposures. A soak time was used for both TBF and $NiCp_2$ pulses to increase the exposure of both precursors to the surface. If a soak was implemented, during the pulse both the purge gas flow and the pump were closed off from the chamber. Following the pulse, both the purge gas source and pump remained isolated from the chamber for the duration of the soak time. This step allowed for an extended period of time for the precursor to remain in contact with the substrate surface. Following the soak, both the purge gas and pump access were reintroduced to the chamber for a set time, allowing for the purging of the reactor chamber.

For deposition of ternary Fe-Al-O films, two schemata were used. In the first, an iron oxide film was deposited by ALD to a thickness of 5-6 nm, and then aluminum oxide was deposited on top of the iron oxide layer. All iron oxide depositions used a 30 s pulse time of TBF, 90 s soak time, and 90 s purge time, but ozone exposure was varied across the experiments. All aluminum oxide ALD was performed using alternating pulses of 2 s of TMA and 2 s of H_2O, with 30 s purge time for each. In the second schema, a supercycle strategy was used to deposit a more homogeneous multilayered film. A single “supercycle” consisted of some number of iron oxide ALD cycles using the above recipe followed by 2 cycles of aluminum oxide. This supercycle was then repeated 10 times, resulting in a film deposited by alternating back and forth

between the iron oxide and aluminum oxide processes. Further details of the supercycle method have been described elsewhere.[14,26,38]

In Situ & In Vacuo Process Characterization

QCM was implemented to probe mass changes *in situ* during the ALD process. QCM measurements were made using a Colnatec Eon-Tempe system with internal thermocouple and heater to control sensor head temperature. To reduce deposition on the rear side of crystal, the backside was sealed off. The process was monitored using a Colnatec universal oscillator and Colnatec Eon control and monitoring package. Temperature and mass gain of the crystal substrate were recorded in tandem at a sample interval of 0.1 seconds.

In situ QMS (SRS RGA200) was used to measure gaseous byproducts of the ALD reactions. The QMS was pumped by a turbomolecular pump separate from the main chamber pump, and measurements were taken by isolating the main pump from the chamber and opening a needle valve to the QMS. QMS monitoring and control was performed through the RGA software package from Stanford Research. High surface-area powder substrates as described above were used in QMS measurements of the ALD process to maximize the surface area available for ALD reaction and thus the signal available from partial pressure of gaseous byproducts. Experiments were performed after the substrate had been thoroughly coated with the ALD material of interest, ensuring measurements probed a growth regime not affected by process nucleation behavior. To collect a measurement, a given reactant exposure was performed by pulsing the reactant followed by a 180 s soak while the pump was isolated to allow for sufficient contact with the porous high surface-area substrate. The TBF pulses were 20 s each, and the ozone pulses were 2 s each. The soak resulted in the accumulation of gaseous

byproducts, after which a gas sample measurement was taken as described above. For measurements where reactant-only cracking patterns were to be measured with no surface reactions, the high surface-area powder was not used, and the reactor temperature was reduced to 85 °C, a minimum temperature to ensure TBF remained volatile but well below the reported ALD window for Fe_2O_3.[31–33] For these experiments, TBF and O_3 pulses were 20 s and 5 s each, respectively, with no soak times, to attempt to reach similar reactant partial pressures as used in the ALD experiments. The QMS was run in full survey mode to scan across an m/z range of 0-200 for all measurements, including both ALD and reactant cracking pattern. Multiple scans were taken over time, and the single scan with the greatest overall intensity was chosen for analysis. Scans were not averaged because intensity varied significantly as a function of scan. In all experiments, the most intense mass spectrum was consistently the second scan, as intensity dropped significantly in further scans as gaseous species were pumped away. Due to the mass transport limitations of fully exposing the high surface-area substrate to the reactants and releasing the byproducts, time-resolved QMS experiments were not performed.

In vacuo XPS was performed to analyze surface species between ALD half-reaction steps without exposing the growth surface to ambient conditions. This measurement was achieved by attaching the cross-flow ALD reactor to a load-lock chamber which was in turn connected to the an ultrahigh vacuum (UHV) chamber with XPS capabilities. To take a measurement after a given exposure was performed in the ALD chamber, the sample holder was transferred through the load-lock into the UHV chamber for XPS analysis without breaking vacuum. Through this procedure, sensitive surface species that may otherwise have been unstable under ambient conditions could be observed. The ALD reactor, load-lock, and UHV chambers were each separated by gate valves. The load-lock and UHV chambers were each pumped by a

turbomolecular pump and the UHV chamber additionally by an ion pump and titanium sublimation pump. During transfers of the sample to the UHV chamber, the load-lock was pumped to below at least $8x10^{-8}$ Torr, and before XPS measurements the UHV chamber was pumped to below at least $2x10^{-9}$ Torr. The XPS unit consisted of a SPECS PHOIBOS hemispherical analyzer and SPECS-50 X-ray source. Measurements in this work used Al Kα radiation. Data was collected in either SpecsLab or SPECS Prodigy software, survey scans were collected with a pass energy of 50 eV, and high-resolution scans were collected with a pass energy of 25 eV. Spectra analysis was performed in the UNIFIT software package, and the reference peak to which all *in vacuo* spectra were shifted to was the Si 2p peak in thermal SiO_2 at 103.5 eV.[40]

In situ spectroscopic ellipsometry (iSE) was performed to gain insight into thickness changes during the ALD process and was performed on a Woollam Co. iSE with a photon energy range of 1.24 eV to 3.10 eV. The iSE source and detector were fixed at a 70° angle to a perpendicular-flow reactor, and the beam was allowed to enter the reactor through quartz windows. To prevent unwanted deposition on the windows, gate valves were installed between the windows and the chamber; these gate valves remained closed at all times except during iSE measurements. Data was analyzed in the Woollam Co. CompleteEASE software package. Details on the models used for each material are given below. For measurements where Al_2O_3 was deposited on top of various substrates, the substrate and growing Al_2O_3 film were modeled separately. The substrate thickness was modeled as it was grown, and its final thickness immediately prior to the start of Al_2O_3 deposition was recorded. During the subsequent Al_2O_3 growth, only the thickness of Al_2O_3 was fit, and the thickness of the substrate was fixed at the previously determined value.

Ex Situ Film Characterization

Variable-angle spectroscopy (VASE, Woollam Co. α-SE spectroscopic ellipsometer) was used to determine *ex situ* film thickness. Measurements were collected with a photon energy range of 1.39-3.25 eV at 65° and 70° angles. Data was modeled in Woollam Co. CompleteEASE software to extract film thickness. Iron oxide films were modeled using a general oscillator layer model containing a Tauc-Lorentz and a Gaussian absorption component. The generation and parameterization of the model has been described previously.[21] Aluminum oxide and nickel oxide materials were both modeled with different Cauchy models based on their optical properties.

Ex situ XPS was performed using a PHI 5000 VersaProbe III with monochromated Al K-α X-ray source to gain information regarding chemical state and elemental composition. An Ar 2500+ gas cluster ion beam was used at 2.5 kV for 4 minutes to remove adventitious carbon species *in situ* prior to XPS measurements. These parameters were chosen based on previous work.[21] Analysis and peak fitting was performed in the MultiPak software package, with a Shirley background for all peaks. Angle-resolved XPS (AR-XPS) was performed in the same instrument by manipulating the angle of the sample stage relative to the hemispherical analyzer.

To analyze atomic arrangements, two-dimensional grazing-incidence wide-angle X-ray scattering (GIWAXS) was performed at the Stanford Synchrotron Radiation Light Source (SSRL) at the SLAC National Accelerator Laboratory using a 2D Rayonix MX225 detector at 150 mm distance. A beam wavelength of 0.976 Å was used at an incidence angle of 0.2°. Data was analyzed in the WxDiff and Igor Nika software packages.[41] X-ray reflectivity (XRR, PANalytical X'Pert PRO X-ray diffractometer) was used to probe film thickness and density.

Measurements were collected over a 2θ range of 0°-8° using a Cu K-α radiation source. Data was modeled and plotted using the PANalytical X'Pert Reflectivity and Igor Motofit software packages.[42]

Results and Discussion

Nickel Oxide and Iron Oxide ALD Process Behavior

To begin understanding the growth mechanism of nickel oxide and to draw comparisons between previous work on iron oxide,[21] the nickel oxide ALD process was first characterized. Saturation curves showing the growth per cycle (GPC) of the nickel oxide ALD process as a function of each reactant exposure are shown in Figure 1. Eventual self-limiting behavior is seen with respect to both reactants, although two noteworthy deviations from typical saturation behavior are observed. First, significant amounts of both ozone and $NiCp_2$ are required to reach saturation. Second, the saturating GPC in this regime is greater than 3.5 Å/cycle, well above the approximate monolayer thickness of 2 Å for the cubic salt structure of NiO.[43,44] These behaviors are similar to those seen in a previous study of iron oxide, which found comparably high saturating GPC and reactant exposures needed to reach saturation, as also illustrated in Figure 1.[21] As with iron oxide, the saturating GPC and required reactant exposures observed here are higher than usually observed in ALD processes,[9,13,14,45] including previous reports of similar NiO process.[28–30] These similarities in saturation behavior, combined with the analogous process chemistries of nickel and iron oxide ALD both using metallocene precursors with ozone, suggest a NiO ALD growth mechanism that may parallel the subsurface oxygen mechanism previously reported for Fe_2O_3.[21]

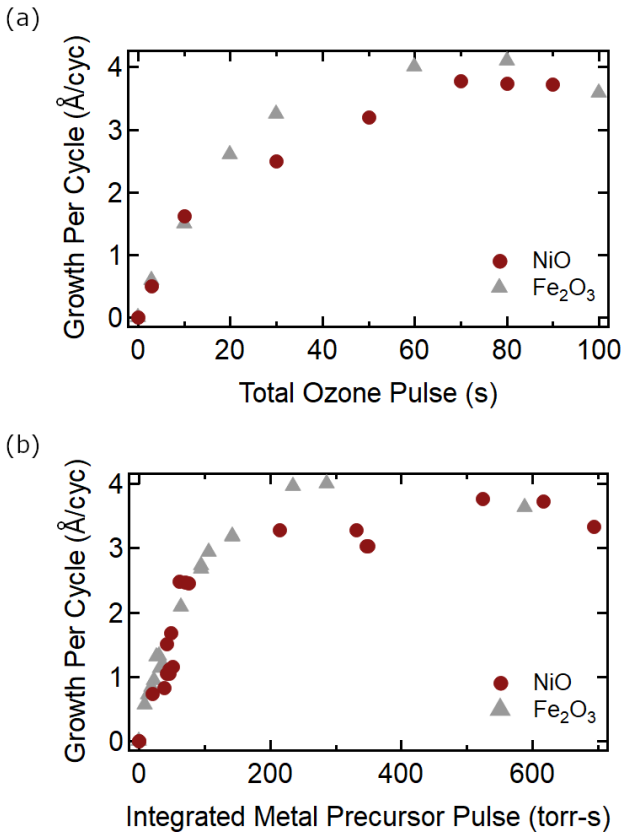

Figure 1: Growth of nickel oxide thin films by ALD as measured by *ex situ* VASE as a function of (a) ozone and (b) $NiCp_2$ exposure. Reference GPC data for Fe_2O_3 is provided for comparison.[21] Saturating $NiCp_2$ exposures were used for each data point in (a), and because the $NiCp_2$ exposure required to reach saturation increases with ozone exposure, the $NiCp_2$ was increased sufficiently to ensure saturation at each point. Similarly, in (b) saturating ozone exposures were used to generate each data point.

The earlier study[21] showed that a consequence of subsurface migration and storage of oxygen in Fe_2O_3 ALD is modulation of the film crystallinity; consequently, the crystalline phase and domain orientation were also investigated for ALD of NiO. Figure 2 contains GIWAXS measurements of ALD NiO films grown with a range of ozone exposures. The ringed structures

are consistent across the range of ozone exposures, with greater relative intensity at specific angles increasing at large ozone exposures. The three rings visible in Figure 2 are all consistent with previous reports and with the cubic rock salt phase of NiO,[38,46] with 2.60 $Å^{-1}$ corresponding to the (111) peak, 3.01 $Å^{-1}$ to (200), and 4.25 $Å^{-1}$ to (220), according to ICCD card 47-1049. With increasing ozone, the (200) ring at 3.01 $Å^{-1}$ shows a localized intensity maximum in the out-of-plane direction, indicating a preferential orientation of the cubic lattice planes parallel to the substrate. The increasingly preferentially oriented (200) peak is paired with the emergence of a comparable preferential orientation for the (111) peak at 2.60 $Å^{-1}$, consistent with the (200) lattice vector aligning out of plane.

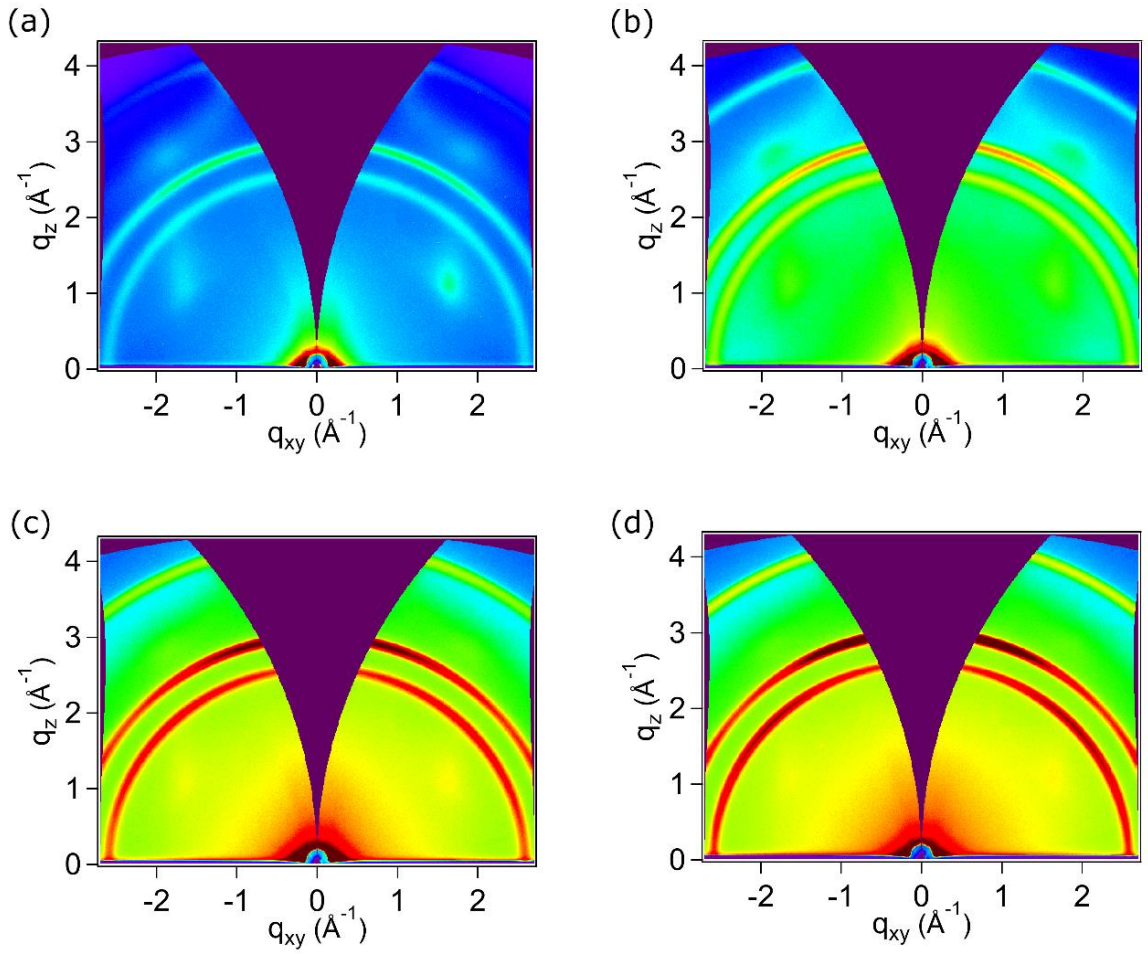

Figure 2. Two-dimensional GIWAXS of ALD NiO films with increasing ozone exposure: (a) 10 s, (b) 30 s, (c) 60 s, (d) 140 s. The thicknesses of each film shown here are 93 Å, 137 Å, 175 Å, and 182 Å, respectively, and the faint background pentagonal pattern is attributed to the silicon substrate. All patterns are plotted with the same color scale for intensity (arbitrary units).

The behaviors observed by GIWAXS for NiO films are similar to those of Fe_2O_3 which showed increasing preferential orientation of the unit cell such that the most facile direction of oxygen diffusion was in the out-of-plane direction.[21] However, there are two key differences between the *ex situ* measurements of NiO and Fe_2O_3: NiO does not undergo a phase transition with increasing ozone exposure, and NiO does not show a loss in crystallinity at high ozone exposure. The former is likely because Fe_2O_3 has many stable phases whereas NiO is reported to exist solely in the cubic rock salt structure, akin to sodium chloride.[38,46,47] Regarding the latter, in Fe_2O_3, the loss of crystallinity at high ozone was attributed to lattice disruption from subsurface storage of oxygen species. There are a number of possible reasons that a loss of crystallinity might not be observed in NiO, including (i) crystallinity loss does occur but only at even higher ozone exposures, (ii) crystallinity loss does occur at the ozone exposures used in Figure 2, but the reservoir is lost and the film reverts back to a crystalline state before the *ex situ* observations are made because the subsurface reactive oxygen species are not stable under ambient conditions, and (iii) crystallinity loss does not occur because subsurface oxygen is not present in large enough quantities. We find (i) to be unlikely because the scattering pattern shown in Figure 2d uses 140 s of ozone per cycle, well above exposures needed to reach the GPC saturation regime in Figure 1a, indicating that additional ozone exposure is not likely to have a significant

effect on the film. To further examine (ii) and (iii) as possibilities, additional film characterization work was performed to compare NiO ALD with Fe_2O_3 ALD.

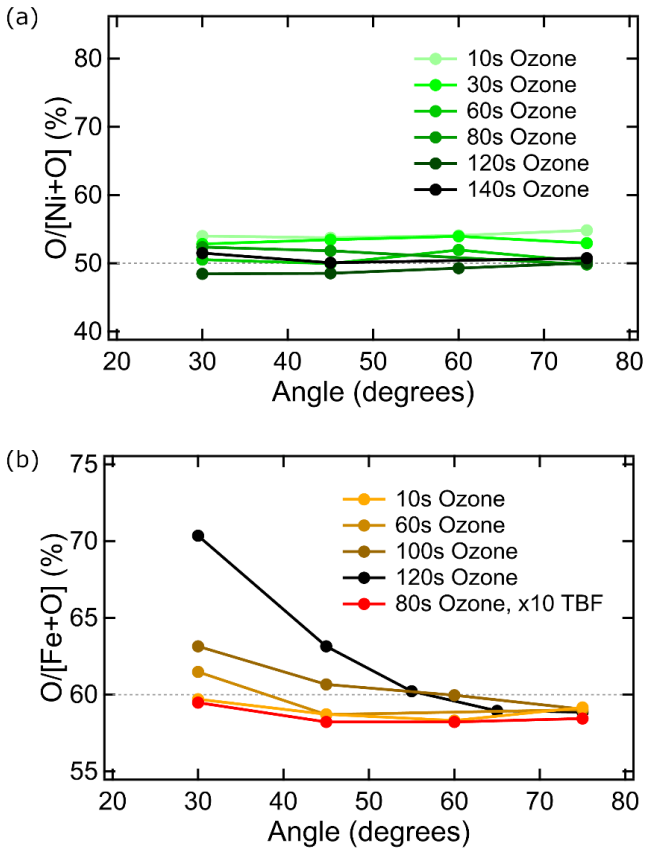

Figure 3. *Ex situ* angle-resolved X-ray photoelectron spectroscopy measurements of ALD (a) NiO and (b) Fe_2O_3 films as a function of ozone exposure, plotting oxygen fraction versus photoelectron detection angle relative to surface plane. Lower angles of incidence are more surface-sensitive. Dashed lines indicate stoichiometric oxygen fraction in bulk NiO and Fe_2O_3. Subfigure (b) reproduced with permission, copyright 2020, WILEY-VCH Verlag GmbH & Co. KGaA, Winheim.[21]

In the previous study of Fe_2O_3, it was found that at larger ozone exposures, the presence of a subsurface oxygen layer could be detected by *ex situ* AR-XPS (Figure 3b) as an oxygen-rich surface region.[21] In contrast, *ex situ* AR-XPS measurements of NiO films synthesized with a range of ozone exposures (Figure 3a) show that even with 140 s of ozone, the elemental oxygen fraction of the film is invariant with detection angle, indicating that the composition is homogeneous as a function of depth. Likewise, XRR does not find a subsurface layer of oxygen in NiO in the same way it was reported to for Fe_2O_3 (Figure S1). Together, these measurements could support either of possibilities (ii) or (iii) described above, since both were performed *ex situ*. Therefore, to further elucidate the behavior of reactive oxygen in the film and avoid possible effects caused by lack of stability in ambient air, *in situ* studies were performed (*vide infra*).

Storage of Oxygen Species

The reaction of ozone with the surface of the growing film can take place in two different ways—a "typical" surface-only reaction or a subsurface reservoir mechanism—and each possibility will result in different overall trends in the mass of the film. If subsurface oxygen is absorbed into the film, the mass of the film will directly *increase* as oxygen species are incorporated into the material. On the other hand, if ozone reacts only at the surface with the products of metalorganic adsorption, as in the typical ALD mechanism, a net *decrease* in mass is expected upon ozone exposure even though oxygen atoms are added to the film surface because the O_3 reaction removes the surface-bound precursor ligands which have greater mass than the added surface oxygen atoms. To differentiate between the two mechanisms, *in situ* QCM was performed for both the Fe_2O_3 and NiO ALD processes during the metallocene precursor and

ozone exposures. Figure 4 illustrates representative QCM mass changes of several ALD cycles of both processes. Significant transient behavior within each pulse is observed due to the pressure and temperature changes taking place on the sensor head during each exposure. As such, net mass changes are found by comparing the mass values only at the beginning and end of a pulse or series of pulses. Although fluctuations caused by temperature changes can cause minor deviations—e.g., evident in comparing the mass gains from the second set of TBF exposures to the first and third—it is apparent in both Figure 4a and Figure 4b that across multiple cycles the broader trends in reactant exposures are consistent.

For both Fe_2O_3 and NiO, the net film mass increases with significant ozone exposure, indicative of oxygen uptake into the film and consistent with a subsurface reservoir mechanism. Moderate differences in the functional form of the mass increase are attributed to different conditions between the two ALD processes. The precursor exposure in the NiO process is lower than in the Fe_2O_3 process due to the significantly lower vapor pressure of the solid $NiCp_2$ compared to the liquid TBF. We partially compensated for this by reducing the number of ozone micropulses and increasing the number of $NiCp_2$ pulses in the NiO process; however, the process still results in a greater relative amount of ozone exposure compared to metal precursor exposure. Consequently, the NiO process runs closer to saturation, as reflected in the gradual bending over of the ozone mass gains seen in Figure 4a.

For the organometallic precursor exposures, both processes generally lead to net mass gains, but the specific QCM behaviors are different. TBF exposures result in a saturating net mass gain over the four micro-exposures (Figure 4b). In addition, the first two ozone doses following TBF exposure yield mass loss. These two behaviors are consistent with self-limiting TBF adsorption followed by surface ligand removal by ozone during the early ozone exposure.

However, subsequent ozone exposure leads to continued mass gain, as discussed above, indicative of oxygen species uptake into the film. $NiCp_2$ exposure, on the other hand, initially leads to mass loss (Figure 4a) followed by gradual mass gain in subsequent pulses. This behavior is consistent with the smaller organometallic exposures per pulse relative to the ozone exposures in the NiO process (due to the lower $NiCp_2$ vapor pressure), because the initial sub-saturating $NiCp_2$ exposures would first withdraw oxygen from the reactive reservoir to combust the precursor ligands, resulting in initial net mass loss. Further exposure will result in mass gain as the reservoir is depleted and Ni and Cp species are deposited on the surface with little removal of oxygen. The incomplete saturation of mass gain with $NiCp_2$ seen in Figure 4a further reflects the low volatility and exposure of the precursor. Overall, the similarity of oxygen uptake behaviors between Fe_2O_3 and NiO in Figure 4 as well as the high GPC and large-exposure saturation conditions in Figure 1 suggest that both ALD processes grow by a subsurface reactive oxygen mechanism and that the reactive species simply cannot be observed *ex situ* in the NiO case.

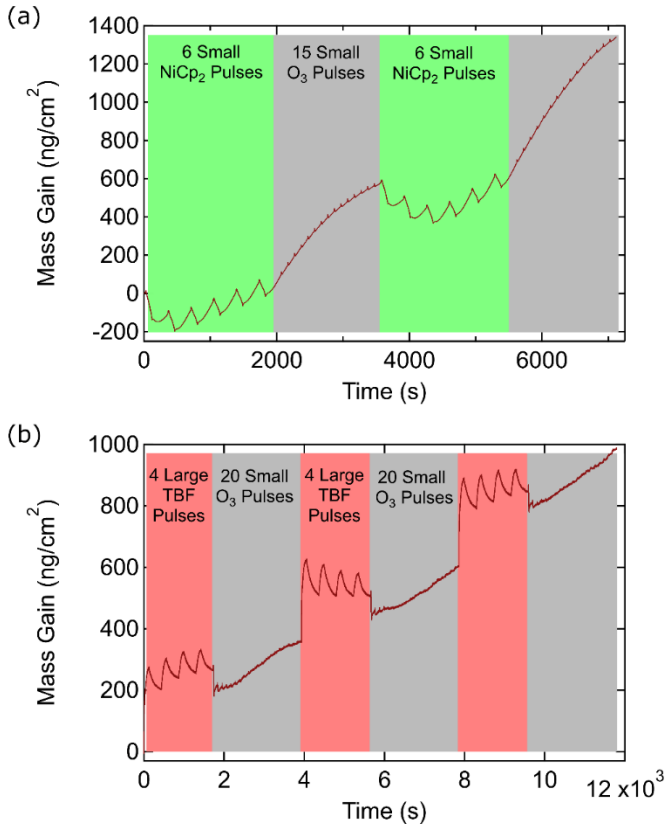

Figure 4. Representative QCM measurements of (a) 2 NiO ALD cycles each with 6 small $NiCp_2$ exposures (30 torr-s each) followed by 15 O_3 micro-exposures and (b) 3 Fe_2O_3 ALD cycles each with 4 large TBF exposures (77 torr-s each) followed by 20 O_3 micro-exposures. In both cases, depositions took place on a QCM crystal already covered with the respective oxide, and significant mass uptakes are observed during the ozone exposures.

To further compare the two processes and investigate the chemical state of the stored oxygen, *in vacuo* XPS was performed. By measuring binding energies and peak structures with XPS as a function of precursor and ozone exposures, information can be gained about changes in species oxidation state and about the identity of oxygen species introduced into the film from ozone. This methodology allows for characterization of reactive species in ways that *ex situ*

methods such as those in Figure 3 and Figure S1were unable to probe. Measurements of Fe_2O_3 ALD resulting from the O 1s and Fe 2p peaks are shown in Figure 5. As seen in Figure 5a, consistent with previous reports[48,49] there are two component oxygen peaks in Fe_2O_3, one at 530 eV and another at 532 eV. By deconvoluting and fitting these two peaks, the ratio of their areas can be calculated as a function of reactant exposure; the results of these calculations are illustrated in Figure 5b. With increasing ozone exposure, the component peak at 530 eV binding energy increases in relative size, and with subsequent TBF exposure it again decreases in size. This suggests the superstoichiometric oxygen introduced into the Fe_2O_3 film from ozone corresponds to species at the 530 eV binding energy state. The literature has mixed hypotheses on the meanings of these two different binding energy peaks, and so the implication of this trend will be discussed further below. Analysis of the Fe 2p peak shows that the binding energy of iron shifts as a function of reactant exposure as well (Figure 5c). Ozone exposure slightly increases the binding energy of the Fe 2p peak, and subsequent TBF exposure decreases the binding energy. While this binding energy increase is less than 1 eV and may not indicate complete film oxidation to a species like Fe^{4+}, it suggests ozone may oxidize some iron species or convert Fe_2O_3 to other forms like FeOOH with higher Fe binding energy, as annotated in Figure 5c.[49,50] Further quantitative analysis or deconvolution of the Fe 2p peak is difficult as the peak structure is very complex.[21,48,50]

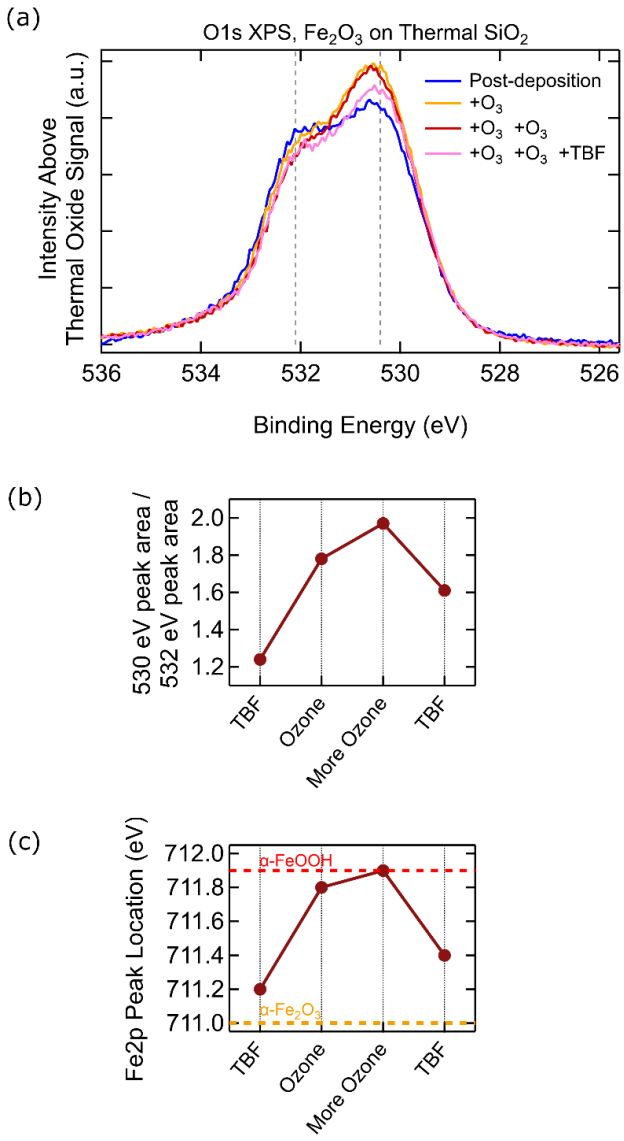

Figure 5. *In vacuo* XPS measurements taken during Fe_2O_3 ALD. (a) O 1s spectra after TBF exposure, two subsequent O_3 exposures, and another TBF exposure, with dashed lines indicating the two component peak locations. (b) Peak ratio of the two deconvoluted O 1s peaks near 530 eV and 532 eV from the spectra in (a). (c) Binding energy shifts in the Fe 2p peak location during the same reactant exposures with the binding energies of α-FeOOH and α-Fe_2O_3 for reference.[49]

Analogous studies were performed on NiO ALD, and the resulting findings are shown in Figure 6. As with Fe_2O_3 in Figure 5a, O 1s spectra of NiO films exhibit two constituent peaks near 530 eV and 532 eV, consistent with previous reports.[38,39,51] The meanings of these two peaks will be discussed in greater detail below. As in Figure 5b, the area ratios of the two oxygen peaks in Figure 6a can be calculated, the results of which are plotted in Figure 6b. A very similar trend to Fe_2O_3 is observed where ozone exposure increases the relative size of the 530 eV binding energy oxygen peak, and then subsequent metalorganic precursor exposure reduces its intensity. We were unable to observe consistent trends in Ni 2p binding energy, and its complex peak structure coupled with changes in structure for different species precludes more quantitative analysis.[38,51] In accordance with the oxygen uptake seen in Figure 4a, observations in Figure 6 further indicate that although oxygen uptake into NiO films during ALD is not observed *ex situ*, the phenomenon does still occur and can be directly observed *in vacuo*. Furthermore, this experiment shows the superstoichiometric oxygen species introduced by ozone in NiO also correspond to the binding energy closer to 530 eV, rather than the higher binding energy oxygen near 532 eV.

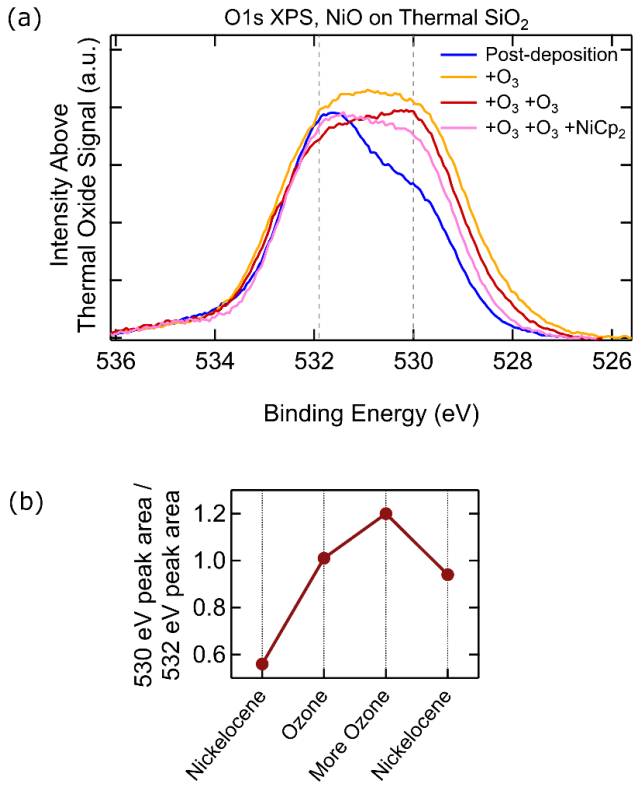

Figure 6. *In vacuo* XPS measurements taken during NiO ALD. (a) O 1s spectra after $NiCp_2$ exposure, two subsequent O_3 exposures, and another $NiCp_2$ exposure, with dashed lines indicating the two component peak locations. (b) Peak ratio of the two deconvoluted O 1s peaks near 530 eV and 532 eV from the spectra in (a).

The results of Figure 5 and Figure 6 suggest a number of possible mechanisms for reactive oxygen species formation during uptake into the oxygen reservoir, including pathways that either oxidize or do not oxidize the metal center. In Fe_2O_3 ALD, species formation resulting in the partial oxidation of Fe metal centers (Figure 5c) could include oxyhydroxides and metastable Fe^{4+} species, which have Fe 2p binding energies of 711.9 eV or higher.[49] The XPS measurements performed here are unable to distinguish between these possible species however,

and additional work such as density functional theory calculations or molecular dynamics simulations could aid in elucidating the likelihoods of these possibilities. While the increase in Fe binding energy indicates oxidative pathways are more likely, with this data alone non-oxidative possibilities cannot be ruled out, so they may also be occurring in tandem with oxidative mechanisms. Non-oxidative pathways consistent with a 530 eV binding energy of introduced oxygen species could include the formation of peroxyl species or oxygen vacancy filling. Since the higher binding energy oxygen component around 532 eV has been attributed to defects and vacancies,[48,51] an increase in the 530 eV to 532 eV peak area ratio with ozone exposure seen in Figure 5b could suggest that the oxygen taken up into the film occupies and fills in these defects and vacancies. These pathways are also consistent with literature reports of NiO for the identities of the 530 eV and 532 eV O 1s peaks. The lower binding energy species has been attributed to NiO primary lattice oxygen, arising from its primary octahedral rock salt structure, with the higher binding energy peak corresponding to defects, vacancies, and hydroxyl species.[38,51] The similar observation of the relative increase of the 530 eV peak with ozone in NiO ALD could therefore also be consistent with the filling of vacancies and defects.

Surface Reaction Mechanism

To investigate the surface reactions of the subsurface oxygen species during the ALD process, *in situ* QMS was performed. QMS was used to analyze the gaseous byproducts of each ALD half-reaction in the Fe_2O_3 process, the results of which are shown in Figure 7. In Figure 7a-c, mass spectra of the background gas and the TBF and O_3 reactants are shown. The background spectrum in Figure 7a contains expected residual species of N_2 from the purge gas and other trace air species such as O_2, CO_2, and H_2O. The ozone cracking pattern in Figure 7b contains

these same species but with partial pressures for O and O_2 that are orders of magnitude larger, as well as a new peak at m/z = 48 corresponding to O_3. A slight increase in the m/z signal for CO_2 is also observed, which may be due to combustion of residual reactor contaminants, but the increase is negligible compared to ALD observations as will be discussed below. The TBF spectrum in Figure 7c contains numerous peaks in the m/z = 50-150 range which are attributed to the many hydrocarbon and iron daughter fragments arising from ionization of the precursor. Notable peaks include the ^{t}Bu-Cp peak at m/z = 121, ^{t}Bu at m/z = 57, and Fe at m/z = 56. A small peak arising from $FeCp_2$ is also observed at m/z = 186. As in Figure 7b, the CO_2 signal in Figure 7c is also increased with respect to the background, but this increase will be shown to be negligible compared to ALD reaction product partial pressures.

Figure 7d shows the partial pressures of CO_2 and O_2, the two most abundant gaseous reaction byproducts, as a function of various ALD pulse conditions. In comparing the QMS intensities of these two species during ozone and TBF exposures under ALD conditions to that of the background, differences are observed. First, CO_2 is present during both exposures at partial pressures above ~10^{-4} Torr (during TBF pulse) and ~10^{-3} Torr (during O_3 pulse), which are significantly larger than the CO_2 contributions from either reactant alone with no ALD reaction (Figure 7b-c) or the background ($1x10^{-6}$—$5x10^{-5}$ Torr, Figure 7a), indicating it is a prominent ALD reaction product. The data show that CO_2 is released in large amounts with ozone pulses, as well as in lesser quantities with TBF pulses. This result signifies complete combustion of hydrocarbon ligands at the surface resulting in the formation of CO_2 gas, consistent with the strong oxidizing nature and plentiful supply of oxygen in ozone. Other potential products from incomplete combustion of TBF, such as cyclopentadienone,[32] were observed in small quantities, but due to the large number of potential species and overlap with the numerous hydrocarbon

peaks inherent to the TBF cracking pattern (Figure 7c), quantitative analysis of these species was not performed.

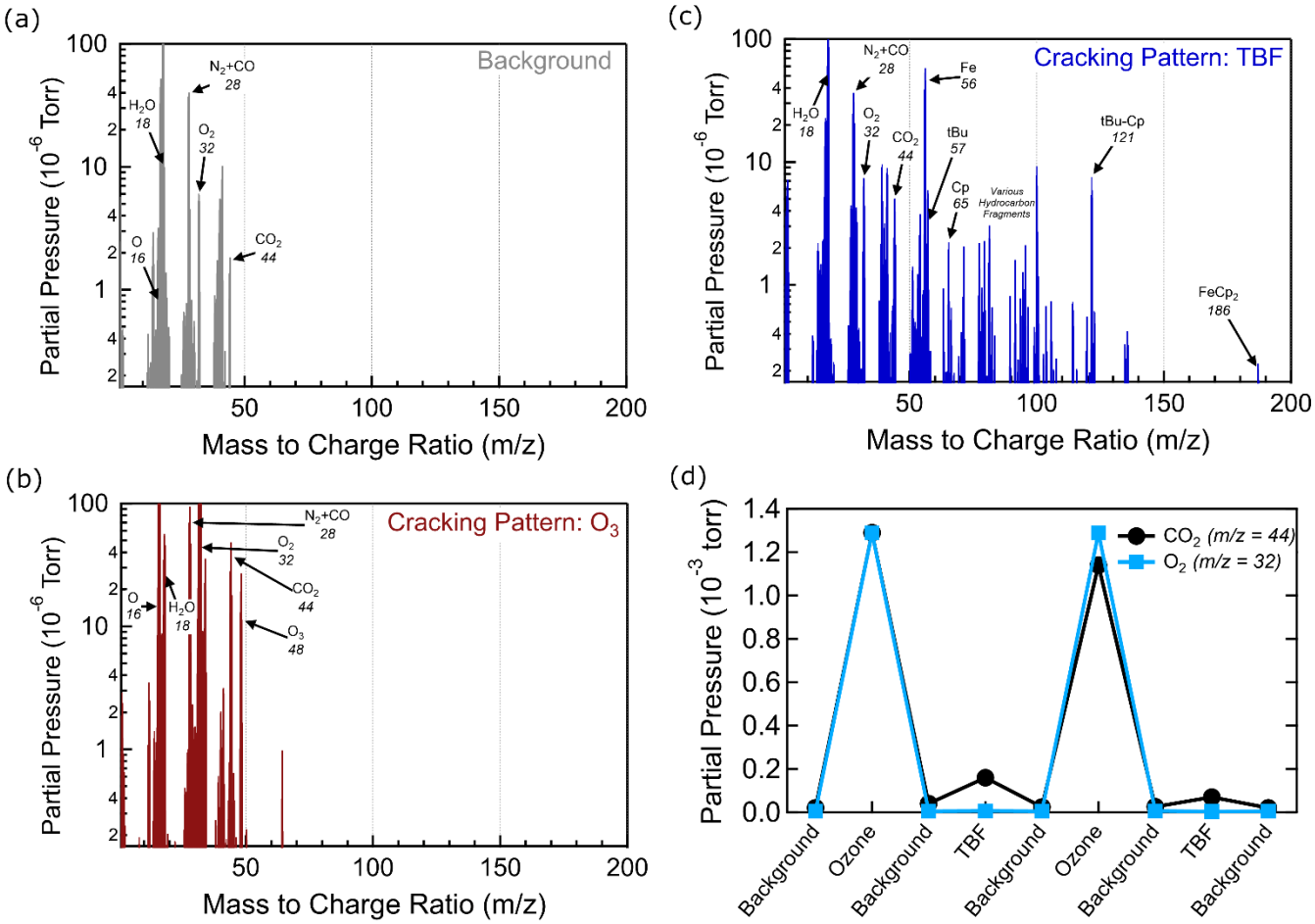

Figure 7. *In situ* QMS data of Fe_2O_3 ALD. Raw QMS spectra shown in semilog form with species annotations include (a) background, (b) cracking pattern of ozone co-reactant only, and (c) cracking pattern of *tert*-butylferrocene precursor only. (d) QMS m/z signal of CO_2 and O_2 species measured under ALD conditions with alternating ozone and TBF exposures, each separated by purges to obtain background values.

It is notable that CO_2 from combustion is present during TBF exposures. This result indicates that enough oxygen must be stored in the film to completely combust TBF ligands upon precursor adsorption. Because of the carbon-rich Cp and ^{t}Bu-Cp rings, each TBF molecule requires 37 oxygen atoms to combust according to the complete combustion reaction $C_5H_5 + (C_4H_9)C_5H_4 + 37O \rightarrow 14CO_2 + 9H_2O$. Therefore, achieving combustion to CO_2 of single monolayer of TBF molecules would require significantly more than a single monolayer of surface oxygen species. Furthermore, since multiple monolayers of Fe_2O_3 are deposited each cycle, both of the Cp ligands in each TBF molecule within the initially deposited monolayers must be eliminated for growth to continue, requiring significant amounts of oxygen. Although incomplete combustion is possible, the observation of CO_2 at significant pressures (~0.1 mTorr, orders of magnitude above the TBF cracking pattern signal) indicates that it is a major reaction product. Hence the observation of CO_2 production during the TBF pulse supports the conclusion that a reservoir of reactive oxygen is present in the subsurface region of the Fe_2O_3 film.

Finally, while O_2 is detected in large quantities during ozone ALD exposures (Figure 7d) as expected from the ozone cracking pattern (Figure 7c), oxygen is not detected above background levels during TBF exposures. This result suggests the reactive subsurface oxygen does not spontaneously leave the film in detectable amounts.

The results in Figure 7 indicating that the ALD surface reaction mechanism of the ozone reaction proceeds through combustion is consistent with previous reports, given that bulky and aromatic Cp rings are unlikely to undergo other forms of reaction like ligand exchange.[14,17] The observation of combustion during the organometallic chemisorption half-reaction as well the ozone half-reaction indicates the subsurface oxygen species are highly reactive and likewise able

to participate in oxidative combustion reactions. While *in situ* QMS experiments were not performed for NiO ALD, we expect the gaseous byproducts to be similar to those of Fe_2O_3, consistent with ligand combustion, since both processes rely on surface passivation through bulky, aromatic Cp ligands and ligand removal through highly oxidative ozone.

Oxygen Reservoir Activation in Other ALD Processes

The observed mechanism of subsurface reactive oxygen driving surface combustion reactions in both Fe_2O_3 and NiO ALD has implications both for these particular processes as well as other ozone- or oxygen plasma-based ALD processes. The role of reactive oxygen reservoirs in other ALD processes is thus investigated here in two ways: (i) comparing the phenomena observed for Fe_2O_3 and NiO to literature reports of other ALD systems to identify similar trends, and (ii) conducting further experiments in which oxygen reservoir ALD processes are combined with additional ALD systems to test whether the oxygen reservoir can activate growth of different processes.

We first examine other ALD oxide processes from the literature. There are reports of systems besides Fe_2O_3 and NiO with growth behaviors in line with a subsurface reactive oxygen reservoir. Recent reports of TiO_2 ALD with oxygen plasma[52,53] built on the initial report of Fe_2O_3[21] and found that with increased exposure to the reactive oxygen plasma superstoichiometric oxygen could be introduced and stored into the film; the authors' reported mechanisms is very similar to that of Fe_2O_3, and as we have shown here, also of NiO. In a different report studying the catalytically activated ALD of Fe_2O_3 using oxygen, it was found that oxygen saturation was lost at higher film thicknesses; the authors hypothesized that the effect was due to a reservoir effect of oxygen species diffusing into the film.[54] Moreover, a study

of manganese oxide ALD using a metallocene precursor with ozone found oxygen uptake by QCM similar to Figure 4. Also similar to findings for NiO and Fe_2O_3, the authors reported an increase in oxygen content in MnO_x corresponding to changes in oxide stoichiometry, high exposures needed to reach saturation, and film phase conversion.[55] On the contrary, deposition of aluminum oxide from trimethylaluminum and ozone does not seem to exhibit this behavior, instead saturating at a sub-monolayer GPC with much lower reactant exposures.[34,35]

The presence of the oxygen reservoir phenomenon in some ozone-based, metal oxide ALD processes but not others raises the question of what chemical, material, and process properties are necessary to cause this subsurface reactive oxygen growth. Some possible contributing factors include the microstructure of the deposited metal oxide, oxygen diffusivity in the deposited material, and the range of oxidation states available to the metal in the deposited film. The observation of a preferential alignment of both Fe_2O_3 and NiO crystalline domains such that the direction of most facile oxygen diffusion is oriented perpendicular to the substrate, in the direction of growth, suggests mobility of oxygen in the material could be a factor.[56,57] Indeed, the diffusion coefficients of oxygen in iron, nickel, and titanium oxides are orders of magnitude larger than that of oxygen through aluminum oxide.[58–61] Relatedly, the materials described here for which a subsurface oxygen growth mechanism is observed—namely iron, nickel, manganese, and titanium oxides—are all crystalline as deposited by ALD, whereas aluminum oxide is amorphous. This correlation suggests the presence of crystalline grain boundaries and their related effect on oxygen mobility through the film may play a role. Additionally, the ability of the metal center in the film to be oxidized and hence accommodate superstoichiometric oxygen may facilitate this subsurface growth mechanism. Iron, manganese, and titanium are all well-known to exist in multiple oxidation states and form various oxides. For

example, manganese oxide can uptake oxygen and convert to higher oxides during ALD, and while nickel typically only has one oxide NiO, it is well-known to exist in higher oxidation states in materials like nickel oxyhydroxide under certain basic or oxidizing conditions.[26,38,39,55,62] Aluminum, on the other hand, has primarily the 3+ oxidation state and its oxide usually exists only as Al_2O_3.[62] Because the uptake of subsurface reactive oxygen may involve oxidation of the metal center, as seen in the XPS spectra for iron oxide ALD in Figure 5, the ability of the metal to coordinate to additional oxygen may be a significant factor in determining if such a mechanism is favorable to occur. Other metal oxides with facile oxygen diffusivity, crystalline structure, and multiple oxygen coordination states may be suitable to grow by an oxygen reservoir mechanism in ALD.

We next turn to design of experiments to test whether the oxygen reservoir can activate growth of a different ALD process conducted on top of the oxygen-rich film. Previous work has observed behaviors consistent such a mechanism. For example, in ternary ALD of $NiAl_xO_y$ in which the component NiO binary process used $NiCp_2$ and ozone, Baker et al. found that growth of Al_2O_3 was enhanced on NiO surfaces and that the films were aluminum-rich compared to compositions predicted by a simple linear combination of the binary GPCs,[38] consistent with the presence of reactive oxygen species near the surface of the NiO that accelerates the Al_2O_3 growth. In another recent example,[63] a study of ternary ALD of $GdFe_xO_y$ found the process was sensitive to ozone exposure and concentration during the Fe_2O_3 portion of the deposition with increased uniformity upon prolonged ozone exposure, consistent with greater exposures needed to reach full saturation; the work also reported superstoichiometric oxygen in Gd_2O_3 deposition, which the authors postulate could be attributed to prolonged ozone exposure as in the previous iron oxide report.[21,63]

Although the earlier work led to speculation about the potential influence of activation by an oxygen reservoir in ternary ALD, no direct study has yet been performed. Here, we test the hypothesis by performing ternary ALD of $FeAl_xO_y$, which is the first report of depositing this material by ALD. Iron aluminum oxide, typically prepared by solution co-precipitation, is a material of interest for ferromagnetic, piezoelectric, catalytic, and adsorption-based contaminant removal applications.[14,64–67] Two types of experiments were performed here to investigate reactive oxygen reservoirs' effects on its synthesis. In the first set of depositions, aluminum oxide was grown on top of different layers of iron oxide synthesized with varying ozone exposures, and the Al_2O_3 growth in the nucleation regime of early cycle numbers was monitored. In the second set of depositions, repeated supercycles alternating between Fe_2O_3 and Al_2O_3 were deposited with varying ozone exposures in the Fe_2O_3 cycles, and effects on overall film growth and composition were characterized.

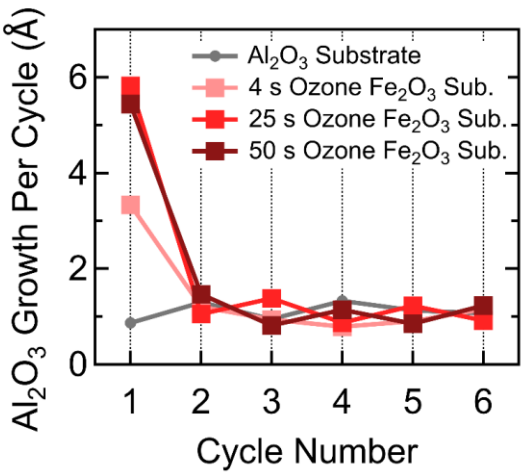

Figure 8. *In situ* spectroscopic ellipsometry measurements of the growth per cycle (GPC) of Al_2O_3 each cycle on different Fe_2O_3 substrates deposited with a range of ozone exposures. The GPC of Al_2O_3 on Al_2O_3 was also measured and is shown as a reference in the gray circles.

For the first set of experiments, results of the growth per cycle of Al_2O_3 on Fe_2O_3 as measured by *in situ* ellipsometry are shown in Figure 8. All Fe_2O_3 substrates were deposited with the same TBF exposure to similar thicknesses of 50-60 Å as described in the Experimental Methods. The figure shows that the GPC of Al_2O_3 during the first ALD cycle is enhanced on ALD Fe_2O_3 compared to growth on Al_2O_3. Furthermore, this growth enhancement increases in magnitude with increased ozone exposure used in the ALD of the underlying Fe_2O_3. Since large ozone exposures lead to increased presence of reactive subsurface oxygen,[21] if that reactive oxygen participates in surface combustion reactions—as it was in the Fe_2O_3 process by QMS—with the TMA precursor, the increased amount of reactive oxygen in the reservoir should correlate with more activated Al_2O_3 growth on the surface. This proposed mechanism is consistent with previous reports of Al_2O_3 ALD using TMA and O_3 indicating that the methyl ligands in TMA can be removed through an oxidation or combustion-type mechanism,[34,68–71] and it also parallels evidence of Al_2O_3 activation on NiO after ozone exposure in ternary ALD of $NiAl_xO_y$.[38] It is notable, however, that in Figure 8 (i) the activation is only present for the first ALD cycle of Al_2O_3 and (ii) the activation does not increase with additional ozone beyond 25 s. The first result is consistent with the observations of Baker et al. in the $NiAl_xO_y$ system of Al_2O_3 activation on NiO.[38] Regarding the second, ozone exposures beyond 25 s have been shown introduce further reactive oxygen into the Fe_2O_3 film,[21] suggesting that the additional reactive oxygen is unable to activate Al_2O_3 growth. We propose that this lack of activation despite the

presence of additional reactive oxygen is explained by the limited mobility of oxygen through Al_2O_3 and the fact that Al_2O_3 does not form its own reactive oxygen reservoirs under ozone exposure. Hence, beyond a threshold thickness of Al_2O_3 deposited on top of the Fe_2O_3 reservoir, reactive oxygen transport to the Al_2O_3 growth surface is blocked through a "capping" phenomenon, inhibiting further growth activation. In their work, Baker et al.[38] observed a growth of the first cycle of Al_2O_3 on NiO of approximately 5 Å with no further activation in future cycles, in line with the 5-6 Å seen in Figure 8 before Al_2O_3 activation plateaus, suggesting that 2-3 monolayers of amorphous Al_2O_3 are sufficient to effectively block further oxygen transport from the underlying reactive oxygen reservoir.

To further characterize how reactive oxygen in the reservoir can influence deposition of ternary films by ALD, a second set of experiments was performed depositing Fe_2O_3 and Al_2O_3 in a supercycle scheme. In the supercycle process for ternary ALD, n_A cycles of binary ALD process A are alternated with n_B cycles of binary ALD process B to deposit a mixed film.[14] Using this cycle number terminology along with the GPCs of each process (g_i) and atomic densities of each material (ρ_i), the atomic composition of the resulting ternary film can be predicted assuming no interaction between the two processes. This result is known as the rule of mixtures,[72] and states that the ideal atomic composition of material A in the final film is given by

$$\text{Atomic Composition of A}(\%) = \frac{\rho_A g_A n_A}{\rho_A g_A n_A + \rho_B g_B n_B} \times 100\% \quad (1)$$

In essence, this relation states that the atomic composition of A is the total amount of material of A deposited per supercycle divided by the total amount of material deposited each supercycle.

In performing the set of supercycle experiments, the number of cycles of Al_2O_3 per supercycle (n_{Al}) was kept constant at 2. The ozone exposure used in Fe_2O_3 cycles was varied, resulting in changes in g_{Fe} between depositions. To correct for this variation, the number of cycles of Fe_2O_3 (n_{Fe}) was tuned each deposition to compensate for changes in GPC such that the total thickness of Fe_2O_3 deposited each supercycle ($g_{Fe}n_{Fe}$) remained similar. After the deposition of each film, the relative atomic composition of Fe and Al was measured using XPS. Since the rule of mixtures predicts the iron atomic concentration relative to Al to be given by Equation 1 where A = Fe and B = Al, this protocol allows for the extraction of the effective growth of Al_2O_3 (g_{Al}) in each process, assuming ρ_{Fe} and ρ_{Al} remain unchanged between experiments. As such, by measuring the final atomic composition of the ternary $FeAl_xO_y$ films, trends between the activated growth of Al_2O_3 (effective increase in g_{Al}) and the process recipe for Fe_2O_3 can be analyzed. Furthermore, because the layer thickness of Fe_2O_3 remains similar across experiments, the changes in average g_{Al} and more likely to be caused by changes in the interaction of oxygen reservoirs in Fe_2O_3 at the surface of Al_2O_3 growth rather than spurious effects arising from significant Fe_2O_3 bilayer thickness changes. This is further supported by alignment of the results calculated below with g_{Al} values in Figure 8, which were grown on much thicker Fe_2O_3 layers of consistent thickness.

The resulting XPS measurements of $FeAl_xO_y$ films deposited with 4 s and 50 s of ozone in Fe_2O_3 ALD cycles are shown in Figure S2, with all peaks consistent with Fe_2O_3, Al_2O_3, and possible mixed species. The final relative Fe:Al composition of the low-ozone film—deposited with 18 sub-cycles of Fe_2O_3 ALD to result in 5.4 Å per supercycle—was 46:54, and the composition of the high-ozone film—deposited with 2 cycles of Fe_2O_3 to result in 7.0 Å per supercycle—was also 46:54. These compositions are both Al-rich compared to the expected Al

compositions of 30-35% if Al_2O_3 were to grow at its unenhanced rate of 1.2 Å/cyc, indicating some degree of enhanced growth in both of these experiments. Since more iron was grown per supercycle in the high-ozone film (7.0 Å versus 5.4 Å), this implies more Al_2O_3 was also deposited in the high-ozone case in order to yield similar overall Fe:Al compositions between the two films. Using atomic densities for Fe in Fe_2O_3 (.0087 $Å^{-3}$) and Al in Al_2O_3 (.010 $Å^{-3}$) calculated from their respective mass densities,[75] the measured GPCs for the Fe_2O_3 processes at low and high ozone exposures (0.6 Å/cyc and 3.5 Å/cyc), the number of cycles of each binary process used each supercycle, and the measured relative atomic compositions from Figure S2a-b, Equation 1 can then be used to calculate the average g_{Al} for each experiment. Doing so yields 2.7 Å/cyc for the supercycle recipe using the 4 s ozone Fe_2O_3 process and 3.5 Å/cyc for the recipe with the 50 s ozone process. Since 2 cycles of Al_2O_3 ALD were performed each supercycle, these results can then be compared to the values of the first two cycles of growth in Figure 8 (3.5 and 1.3 Å/cyc for 4 s ozone, and 5.5 and 1.3 Å/cyc for 50 s ozone), and indeed they align with the average growths of Al_2O_3 on each type of Fe_2O_3 substrate (2.4 and 3.4 Å/cyc, respectively). The consistency of this enhancement indicates that the growth activations under the higher ozone exposure conditions (Figure 8) take place in every single supercycle to enhance the growth Al_2O_3, producing the compositions in Figure S2 for the complete ternary $FeAl_xO_y$ films. This enhancement, reflected in finding a g_{Al} in the ternary deposition larger than that of simple growth of Al_2O_3 on itself, means Fe-Al-O compositions will deviate from those predicted by the rule of mixtures applied simply to the respective binary growth rates. Combined with the fact that the enhancement in Fe-Al-O is similar to that observed in Ni-Al-O[38] as well as many other ternary processes[14], this result stresses the importance of rigorous process characterization in multicomponent systems to account for growth deviations and accurate composition control.[14]

Through these two sets of experiments, we have demonstrated that subsurface oxygen reservoirs present in some ozone-based, metal oxide ALD processes can be used to activate the nucleation of subsequent ALD processes during the deposition of mixed materials. The proof-of-concept experiments also demonstrate the first report of $FeAl_xO_y$ deposited by ALD and the critical influence of ozone on the resulting composition and properties of the films. This activation mechanism could be generalizable to other mixed-material systems as well. There are many reports of ternary ALD processes that have been limited in their ability to achieve desired atomic compositions due to difficulties nucleating and growing one binary ALD process on top of the other. A prime example of such processes is those containing silicates[14,76] since SiO_2 is often difficult to grow on its own.[77,78] In multicomponent ALD processes such as these, persisting reactive oxygen species could be used to activate the growth of otherwise unreactive precursors, opening the door to a much wider variety of material syntheses and compositional ranges. Combustion reactions like those confirmed by the CO_2 mass detection in Figure 7 are a robust class of co-reactant reactions,[14,17] meaning the enhancement processes for Al_2O_3 leveraged in this work could also enhance many other ALD processes proceeding by combustion. Furthermore, since ozone and oxygen plasmas are widely used co-reactants in multicomponent ALD,[14] the subsurface activation mechanism could be applied to a wide variety of different systems.

Conclusion

NiO and Fe_2O_3 ALD processes using metallocene precursors with ozone were investigated to probe the chemical mechanisms involved in reactive oxygen uptake and storage in these systems. NiO exhibited similar high-exposure and high-GPC saturation behavior to

Fe_2O_3, and two-dimensional GIWAXS measurements confirmed that increasing ozone in the NiO ALD process resulted in preferential orientation of the crystalline domains in the out-of-plane direction, similar to Fe_2O_3. *In situ* QCM observed significant mass uptake into the film upon extended ozone exposures in both ALD processes, and *in vacuo* XPS measurements revealed increased oxygen content with binding energy around 530 eV after ozone pulses. The oxygen reservoir species could possibly include peroxyls or oxygen vacancy or defect filling. In Fe_2O_3 ALD, iron slightly oxidized with ozone exposure, potentially due to the formation of oxyhydroxides or metastable Fe^{4+} species. *In situ* QMS found that in Fe_2O_3 ALD, oxygen reservoirs are able to fully combust organic ligands during TBF exposures, similar to the combustion mechanism taking place in the ozone reaction. Unlike for Fe_2O_3, *ex situ* methods such as XRR, XPS, and GIWAXS were unable to directly observe oxygen reservoirs in NiO, suggesting they are less stable and revert to stoichiometric NiO under ambient conditions.

Finally, the reactive oxygen reservoir mechanism was applied to $FeAl_xO_y$, a not-yet-reported ternary ALD process. By combining Fe_2O_3 and Al_2O_3 ALD, it was found that the first cycle of Al_2O_3 ALD is enhanced on Fe_2O_3 surfaces, up to five-fold, with increasing enhancement with greater ozone exposure used in the Fe_2O_3 ALD. However, Al_2O_3 enhancement did not increase past 25 s of ozone exposure, plateauing at a GPC of 5-6 Å/cyc, possibly due to a capping phenomenon whereby the Al_2O_3 blocks reactive oxygen transport. When a ternary $FeAl_xO_y$ film was made by alternating the processes in supercycles, the enhancement effects were consistent in each supercycle, resulting in films that were aluminum-rich compared to that predicted by the rule of mixtures. These mechanistic investigations of active oxygen reservoir growth in multiple oxide processes give insight into the generalization and application of the

phenomenon to other ALD systems and processes, including possible multicomponent processes where nucleation could otherwise be difficult.

Acknowledgements

This work was supported by the Department of Energy under Award Number DE-SC0004782. J.R.S. was also supported by a National Science Foundation Graduate Research Fellowship under Grant No. 1656518. Part of this work was performed at the Stanford Nano Shared Facilities (SNSF), supported by the National Science Foundation under award ECCS-1542152. Use of the Stanford Synchrotron Radiation Lightsource, SLAC National Accelerator Laboratory, is supported by the U.S. Department of Energy, Office of Science, Office of Basic Energy Sciences under Contract No. DE-AC02-76SF00515.

Conflict of Interest

The authors declare no conflict of interest.

Supporting Information

Supporting information containing figures and text is available in a separate document.

References

(1) Peng, Q.; Lewis, J. S.; Hoertz, P. G.; Glass, J. T.; Parsons, G. N. Atomic Layer Deposition for Electrochemical Energy Generation and Storage Systems. *J. Vac. Sci. Technol. A Vacuum, Surfaces, Film.* **2012**, *30* (1), 010803. https://doi.org/10.1116/1.3672027.

(2) Asundi, A. S.; Raiford, J. A.; Bent, S. F. Opportunities for Atomic Layer Deposition in Emerging Energy Technologies. *ACS Energy Lett.* **2019**, *4* (4), 908–925. https://doi.org/10.1021/acsenergylett.9b00249.

(3) Raiford, J. A.; Oyakhire, S. T.; Bent, S. F. Applications of Atomic Layer Deposition and Chemical Vapor Deposition for Perovskite Solar Cells. *Energy Environ. Sci.* **2020**, *13* (7), 1997–2023. https://doi.org/10.1039/D0EE00385A.

(4) Serrano, E.; Rus, G.; García-Martínez, J. Nanotechnology for Sustainable Energy. *Renew. Sustain. Energy Rev.* **2009**, *13* (9), 2373–2384. https://doi.org/10.1016/J.RSER.2009.06.003.

(5) Qu, X.; Alvarez, P. J. J.; Li, Q. Applications of Nanotechnology in Water and Wastewater Treatment. *Water Res.* **2013**, *47* (12), 3931–3946. https://doi.org/10.1016/J.WATRES.2012.09.058.

(6) Roco, M. C. Nanotechnology: Convergence with Modern Biology and Medicine. *Curr. Opin. Biotechnol.* **2003**, *14* (3), 337–346. https://doi.org/10.1016/S0958-1669(03)00068-5.

(7) Heerema, S. J.; Dekker, C. Graphene Nanodevices for DNA Sequencing. *Nat. Nanotechnol. 2016 112* **2016**, *11* (2), 127–136. https://doi.org/10.1038/NNANO.2015.307.

(8) Shendure, J.; Ji, H. Next-Generation DNA Sequencing. *Nat. Biotechnol.* **2008**, *26* (10),

1135–1145. https://doi.org/10.1038/nbt1486.

(9) George, S. M. Atomic Layer Deposition: An Overview. *Chem. Rev.* **2010**, *110* (1), 111–131. https://doi.org/10.1021/cr900056b.

(10) Parsons, G. N.; Clark, R. D. Area-Selective Deposition: Fundamentals, Applications, and Future Outlook. *Chem. Mater.* **2020**, *32* (12), 4920–4953. https://doi.org/10.1021/ACS.CHEMMATER.0C00722.

(11) Whitesides, G. M. Nanoscience, Nanotechnology, and Chemistry. *Small* **2005**, *1* (2), 172–179. https://doi.org/10.1002/SMLL.200400130.

(12) Anceau, F. Past, Present and Future of Microprocessors. In *Design of Systems on a Chip: Design and Test*; Springer US: Boston, MA, 2006; pp 65–82. https://doi.org/10.1007/0-387-32500-X_4.

(13) Johnson, R. W.; Hultqvist, A.; Bent, S. F. A Brief Review of Atomic Layer Deposition: From Fundamentals to Applications. *Mater. Today* **2014**, *17* (5), 236–246. https://doi.org/10.1016/J.MATTOD.2014.04.026.

(14) Mackus, A. J. M.; Schneider, J. R.; MacIsaac, C.; Baker, J. G.; Bent, S. F. Synthesis of Doped, Ternary, and Quaternary Materials by Atomic Layer Deposition: A Review. *Chem. Mater.* **2019**, *31* (4), 1142–1183. https://doi.org/10.1021/acs.chemmater.8b02878.

(15) Coll, M.; Napari, M. Atomic Layer Deposition of Functional Multicomponent Oxides. *APL Mater.* **2019**, *7* (11), 110901. https://doi.org/10.1063/1.5113656.

(16) Zaera, F. The Surface Chemistry of Atomic Layer Depositions of Solid Thin Films. *J. Phys. Chem. Lett.* **2012**, *3* (10), 1301–1309. https://doi.org/10.1021/jz300125f.

(17) Richey, N. E.; de Paula, C.; Bent, S. F. Understanding Chemical and Physical Mechanisms in Atomic Layer Deposition. *J. Chem. Phys.* **2020**, *152* (4), 040902. https://doi.org/10.1063/1.5133390.

(18) Schneider, J. R.; Paula, C.; Lewis, J.; Woodruff, J.; Raiford, J. A.; Bent, S. F. The Importance of Decarbonylation Mechanisms in the Atomic Layer Deposition of High-Quality Ru Films by Zero-Oxidation State Ru(DMBD)(CO) 3. *Small* **2022**, 2105513. https://doi.org/10.1002/smll.202105513.

(19) Thimsen, E.; Peng, Q.; Martinson, A. B. F.; Pellin, M. J.; Elam, J. W. Ion Exchange in Ultrathin Films of Cu_2S and ZnS under Atomic Layer Deposition Conditions. *Chem. Mater.* **2011**, *23* (20), 4411–4413. https://doi.org/10.1021/cm201412p.

(20) Lancaster, D. K.; Sun, H.; George, S. M. Atomic Layer Deposition of Zn(O,S) Alloys Using Diethylzinc with H_2O and H_2S: Effect of Exchange Reactions. *J. Phys. Chem. C* **2017**, *121* (34), 18643–18652. https://doi.org/10.1021/acs.jpcc.7b05361.

(21) Schneider, J. R.; Baker, J. G.; Bent, S. F. The Influence of Ozone: Superstoichiometric Oxygen in Atomic Layer Deposition of Fe2O3 Using Tert -Butylferrocene and O3. *Adv. Mater. Interfaces* **2020**, *7* (11), 2000318. https://doi.org/10.1002/admi.202000318.

(22) Espejo, A. P.; Zierold, R.; Gooth, J.; Dendooven, J.; Detavernier, C.; Escrig, J.; Nielsch, K. Magnetic and Electrical Characterization of Nickel-Rich NiFe Thin Films Synthesized by Atomic Layer Deposition and Subsequent Thermal Reduction. *Nanotechnology* **2016**, *27* (34), 345707. https://doi.org/10.1088/0957-4484/27/34/345707.

(23) Chong, Y. T.; Yau, E. M. Y.; Nielsch, K.; Bachmann, J. Direct Atomic Layer Deposition of Ternary Ferrites with Various Magnetic Properties. *Chem. Mater.* **2010**, *22* (24), 6506–

6508. https://doi.org/10.1021/cm102600m.

(24) Lie, M.; Nilsen, O.; Fjellvåg, H.; Kjekshus, A. Growth of La 1−x Sr x FeO 3 Thin Films by Atomic Layer Deposition. *Dalt. Trans.* **2009**, No. 3, 481–489. https://doi.org/10.1039/B809974J.

(25) Lie, M.; Barnholt Klepper, K.; Nilsen, O.; Fjellvåg, H.; Kjekshus, A. Growth of Iron Cobalt Oxides by Atomic Layer Deposition. *Dalt. Trans.* **2008**, 253–259. https://doi.org/10.1039/b711718n.

(26) Baker, J. G.; Schneider, J. R.; de Paula, C.; Mackus, A. J. M.; Bent, S. F. Identification of Highly Active Surface Iron Sites on Ni(OOH) for the Oxygen Evolution Reaction by Atomic Layer Deposition. *J. Catal.* **2021**, *394*, 476–485. https://doi.org/10.1016/j.jcat.2020.09.035.

(27) Seim, H.; Mölsä, H.; Nieminen, M.; Fjellvåg, H.; Niinistö, L. Deposition of LaNiO3 Thin Films in an Atomic Layer Epitaxy Reactor. *J. Mater. Chem.* **1997**, *7* (3), 449–454. https://doi.org/10.1039/a606316k.

(28) Lu, H. L.; Scarel, G.; Li, X. L.; Fanciulli, M. Thin MnO and NiO Films Grown Using Atomic Layer Deposition from Ethylcyclopentadienyl Type of Precursors. *J. Cryst. Growth* **2008**, *310* (24), 5464–5468. https://doi.org/10.1016/j.jcrysgro.2008.08.031.

(29) Lu, H. L.; Scarel, G.; Wiemer, C.; Perego, M.; Spiga, S.; Fanciulli, M.; Pavia, G. Atomic Layer Deposition of NiO Films on Si(100) Using Cyclopentadienyl-Type Compounds and Ozone as Precursors. *J. Electrochem. Soc.* **2008**, *155* (10), H807. https://doi.org/10.1149/1.2965456.

(30) Bachmann, J.; Zolotaryov, A.; Albrecht, O.; Goetze, S.; Berger, A.; Hesse, D.; Novikov, D.; Nielsch, K. Stoichiometry of Nickel Oxide Films Prepared by ALD. *Chem. Vap. Depos.* **2011**, *17* (7–9), 177–180. https://doi.org/10.1002/cvde.201004300.

(31) Li, X.; Fan, N. C.; Fan, H. J. A Micro-Pulse Process of Atomic Layer Deposition of Iron Oxide Using Ferrocene and Ozone Precursors and Ti-Doping. *Chem. Vap. Depos.* **2013**, *19* (4–6), 104–110. https://doi.org/10.1002/cvde.201207030.

(32) Martinson, A. B. F.; Devries, M. J.; Libera, J. A.; Christensen, S. T.; Hupp, J. T.; Pellin, M. J.; Elam, J. W. Atomic Layer Deposition of Fe2O3 Using Ferrocene and Ozone. *J. Phys. Chem. C* **2011**, *115* (10), 4333–4339. https://doi.org/10.1021/jp110203x.

(33) Ramachandran, R. K.; Dendooven, J.; Detavernier, C. Plasma Enhanced Atomic Layer Deposition of Fe2O3 Thin Films. *J. Mater. Chem. A* **2014**, *2* (27), 10662. https://doi.org/10.1039/c4ta01486c.

(34) Kim, J.; Chakrabarti, K.; Lee, J.; Oh, K.-Y.; Lee, C. Effects of Ozone as an Oxygen Source on the Properties of the Al2O3 Thin Films Prepared by Atomic Layer Deposition. *Mater. Chem. Phys.* **2003**, *78* (3), 733–738. https://doi.org/10.1016/S0254-0584(02)00375-9.

(35) Kim, S. K.; Hwang, C. S. Atomic-Layer-Deposited Al2O3 Thin Films with Thin SiO2 Layers Grown by in Situ O3 Oxidation. *J. Appl. Phys.* **2004**, *96* (4), 2323. https://doi.org/10.1063/1.1769090.

(36) Profijt, H. B.; Potts, S. E.; Sanden, M. C. M. van de; Kessels, W. M. M. Plasma-Assisted Atomic Layer Deposition: Basics, Opportunities, and Challenges. *J. Vac. Sci. Technol. A Vacuum, Surfaces, Film.* **2011**, *29* (5), 050801. https://doi.org/10.1116/1.3609974.

(37) Knoops, H. C. M.; Faraz, T.; Arts, K.; Kessels, W. M. M. (Erwin). Status and Prospects of Plasma-Assisted Atomic Layer Deposition. *J. Vac. Sci. Technol. A Vacuum, Surfaces, Film.* **2019**, *37* (3), 030902. https://doi.org/10.1116/1.5088582.

(38) Baker, J. G.; Schneider, J. R.; Raiford, J. A.; Paula, C. de; Bent, S. F. Nucleation Effects in the Atomic Layer Deposition of Nickel–Aluminum Oxide Thin Films. *Chem. Mater.* **2020**, *32* (5), 1925–1936. https://doi.org/10.1021/acs.chemmater.9b04630.

(39) Baker, J. G.; Schneider, J. R.; Garrido Torres, J. A.; Singh, J. A.; MacKus, A. J. M.; Bajdich, M.; Bent, S. F. The Role of Aluminum in Promoting Ni-Fe-OOH Electrocatalysts for the Oxygen Evolution Reaction. *ACS Appl. Energy Mater.* **2019**, *2* (5). https://doi.org/10.1021/acsaem.9b00265.

(40) Moulder, J.; Stickle, W.; Sobol, W.; Bomben, K. D. *Handbook of X-Ray Photoelectron Spectroscopy*; Perkin-Elmer Corporation: Eden Prairie, MN, USA, 1992.

(41) Ilavsky, J. Nika: Software for Two-Dimensional Data Reduction. *J. Appl. Crystallogr.* **2012**, *45* (2), 324–328. https://doi.org/10.1107/S0021889812004037.

(42) Nelson, A. Co-Refinement of Multiple-Contrast Neutron/X-Ray Reflectivity Data Using MOTOFIT. *J. Appl. Crystallogr.* **2006**, *39* (2), 273–276. https://doi.org/10.1107/S0021889806005073.

(43) Cairns, R. W.; Ott, E. X-Ray Studies of the System Nickel—Oxygen—Water. I. Nickelous Oxide and Hydroxide1. *J. Am. Chem. Soc.* **2002**, *55* (2), 527–533. https://doi.org/10.1021/JA01329A013.

(44) Cheetham, A. K.; Hope, D. A. O. Magnetic Ordering and Exchange Effects in the

Antiferromagnetic Solid Solutions. *Phys. Rev. B* **1983**, *27* (11), 6964–6967. https://doi.org/10.1103/PhysRevB.27.6964.

(45) Miikkulainen, V.; Leskelä, M.; Ritala, M.; Puurunen, R. L. Crystallinity of Inorganic Films Grown by Atomic Layer Deposition: Overview and General Trends. *J. Appl. Phys.* **2013**, *113* (2), 021301. https://doi.org/10.1063/1.4757907.

(46) El-Kemary, M.; Nagy, N.; El-Mehasseb, I. Nickel Oxide Nanoparticles: Synthesis and Spectral Studies of Interactions with Glucose. *Mater. Sci. Semicond. Process.* **2013**, *16* (6), 1747–1752. https://doi.org/10.1016/j.mssp.2013.05.018.

(47) Anthony, J. W. *Handbook of Mineralogy*; Mineral Data Pub, 1990.

(48) Biesinger, M. C.; Payne, B. P.; Grosvenor, A. P.; Lau, L. W. M.; Gerson, A. R.; Smart, R. S. C. Resolving Surface Chemical States in XPS Analysis of First Row Transition Metals, Oxides and Hydroxides: Cr, Mn, Fe, Co and Ni. *Appl. Surf. Sci.* **2011**, *257* (7), 2717–2730. https://doi.org/10.1016/j.apsusc.2010.10.051.

(49) McIntyre, N. S.; Zetaruk, D. G. X-Ray Photoelectron Spectroscopic Studies of Iron Oxides. *Anal. Chem.* **1977**, *49* (11), 1521–1529. https://doi.org/10.1021/ac50019a016.

(50) Grosvenor, A. P.; Kobe, B. A.; Biesinger, M. C.; McIntyre, N. S. Investigation of Multiplet Splitting of Fe 2p XPS Spectra and Bonding in Iron Compounds. *Surf. Interface Anal.* **2004**, *36* (12), 1564–1574. https://doi.org/10.1002/SIA.1984.

(51) Biesinger, M. C.; Payne, B. P.; Lau, L. W. M.; Gerson, A.; Smart, R. S. C. X-Ray Photoelectron Spectroscopic Chemical State Quantification of Mixed Nickel Metal, Oxide and Hydroxide Systems. *Surf. Interface Anal.* **2009**, *41* (4), 324–332.

https://doi.org/10.1002/sia.3026.

(52) Chiappim, W.; Testoni, G.; Miranda, F.; Fraga, M.; Furlan, H.; Saravia, D. A.; Sobrinho, A. da S.; Petraconi, G.; Maciel, H.; Pessoa, R. Effect of Plasma-Enhanced Atomic Layer Deposition on Oxygen Overabundance and Its Influence on the Morphological, Optical, Structural, and Mechanical Properties of Al-Doped TiO2 Coating. *Micromachines* **2021**, *12* (6), 588. https://doi.org/10.3390/mi12060588.

(53) Chiappim, W.; Fraga, M. A.; Maciel, H. S.; Pessoa, R. S. An Experimental and Theoretical Study of the Impact of the Precursor Pulse Time on the Growth Per Cycle and Crystallinity Quality of TiO2 Thin Films Grown by ALD and PEALD Technique. *Front. Mech. Eng.* **2020**, *6*, 80. https://doi.org/10.3389/fmech.2020.551085.

(54) Singh, J. A.; Thissen, N. F. W.; Kim, W.-H.; Johnson, H.; Kessels, W. M. M.; Bol, A. A.; Bent, S. F.; Mackus, A. J. M. Area-Selective Atomic Layer Deposition of Metal Oxides on Noble Metals through Catalytic Oxygen Activation. *Chem. Mater.* **2018**, *30* (3), 663–670. https://doi.org/10.1021/acs.chemmater.7b03818.

(55) Young, M. J.; Hare, C. D.; Cavanagh, A. S.; Musgrave, C. B.; George, S. M. Rapid Growth of Crystalline Mn 5 O 8 by Self-Limited Multilayer Deposition Using Mn(EtCp) 2 and O 3. *ACS Appl. Mater. Interfaces* **2016**, *8* (28), 18560–18569. https://doi.org/10.1021/acsami.6b04529.

(56) Sabioni, A. C. S.; Huntz, A. M.; Daniel, A. M. J. M.; MacEdo, W. A. A. Measurement of Iron Self-Diffusion in Hematite Single Crystals by Secondary Ion-Mass Spectrometry (SIMS) and Comparison with Cation Self-Diffusion in Corundum-Structure Oxides. *Philos. Mag.* **2005**, *85* (31), 3643–3658. https://doi.org/10.1080/14786430500323795.

(57) Hallström, S.; Höglund, L.; Ågren, J. Modeling of Iron Diffusion in the Iron Oxides Magnetite and Hematite with Variable Stoichiometry. *Acta Mater.* **2011**, *59* (1), 53–60. https://doi.org/10.1016/j.actamat.2010.08.032.

(58) Heuer, A. H. Oxygen and Aluminum Diffusion in α-Al2O3: How Much Do We Really Understand? *J. Eur. Ceram. Soc.* **2008**, *28* (7), 1495–1507. https://doi.org/10.1016/J.JEURCERAMSOC.2007.12.020.

(59) Takada, J.; Adachi, M. Determination of Diffusion Coefficient of Oxygen in α-Iron from Internal Oxidation Measurements in Fe-Si Alloys. *J. Mater. Sci. 1986 216* **1986**, *21* (6), 2133–2137. https://doi.org/10.1007/BF00547959.

(60) Unutulmazsoy, Y.; Merkle, R.; Fischer, D.; Mannhart, J.; Maier, J. The Oxidation Kinetics of Thin Nickel Films between 250 and 500 °C. *Phys. Chem. Chem. Phys.* **2017**, *19* (13), 9045–9052. https://doi.org/10.1039/C7CP00476A.

(61) Rosa, C. J. Oxygen Diffusion in Alpha and Beta Titanium in the Temperature Range of 932° to 1142°C. *Metall. Trans. 1970 19* **1970**, *1* (9), 2517–2522. https://doi.org/10.1007/BF03038377.

(62) Greenwood, N. N.; Earnshaw, A. *Chemistry of the Elements*, 2nd Editio.; Butterworth-Heinemann: Oxford, United Kingdom, 1997.

(63) Yu, P.; Beer, S. M. J.; Devi, A.; Coll, M. Fabrication of Gd x Fe y O z Films Using an Atomic Layer Deposition-Type Approach. *CrystEngComm* **2021**, *23* (3), 730–740. https://doi.org/10.1039/D0CE01252A.

(64) Bouree, F.; Baudour, J. L.; Elbadraoui, E.; Musso, J.; Laurent, C.; Rousset, A. Crystal and

Magnetic Structure of Piezoelectric, Ferrimagnetic and Magnetoelectric Aluminium Iron Oxide FeAlO3 from Neutron Powder Diffraction. *urn:issn:0108-7681* **1996**, *52* (2), 217–222. https://doi.org/10.1107/S0108768195010330.

(65) Liu, L.; Cui, Z.; Ma, Q.; Cui, W.; Zhang, X. One-Step Synthesis of Magnetic Iron–Aluminum Oxide/Graphene Oxide Nanoparticles as a Selective Adsorbent for Fluoride Removal from Aqueous Solution. *RSC Adv.* **2016**, *6* (13), 10783–10791. https://doi.org/10.1039/C5RA23676B.

(66) Sharpley, A. N. Soil Phosphorus Extracted By Iron-Aluminum-Oxide-Impregnated Filter Paper. *Soil Sci. Soc. Am. J.* **1991**, *55* (4), 1038–1041. https://doi.org/10.2136/SSSAJ1991.03615995005500040025X.

(67) Jeong, Y.; Fan, M.; Singh, S.; Chuang, C. L.; Saha, B.; Hans van Leeuwen, J. Evaluation of Iron Oxide and Aluminum Oxide as Potential Arsenic(V) Adsorbents. *Chem. Eng. Process. - Process Intensif.* **2007**, *46* (10), 1030–1039. https://doi.org/10.1016/J.CEP.2007.05.004.

(68) Goldstein, D. N.; McCormick, J. A.; George, S. M. Al2O3 Atomic Layer Deposition with Trimethylaluminum and Ozone Studied by in Situ Transmission FTIR Spectroscopy and Quadrupole Mass Spectrometry. *J. Phys. Chem. C* **2008**, *112* (49), 19530–19539. https://doi.org/10.1021/JP804296A.

(69) Elliott, S. D.; Scarel, G.; Wiemer, C.; Fanciulli, M.; Pavia, G. Ozone-Based Atomic Layer Deposition of Alumina from TMA: Growth, Morphology, and Reaction Mechanism. *Chem. Mater.* **2006**, *18* (16), 3764–3773. https://doi.org/10.1021/CM0608903.

(70) Rai, V. R.; Vandalon, V.; Agarwal, S. Surface Reaction Mechanisms during Ozone and

Oxygen Plasma Assisted Atomic Layer Deposition of Aluminum Oxide. *Langmuir* **2010**, *26* (17), 13732–13735. https://doi.org/10.1021/la101485a.

(71) Rai, V. R.; Vandalon, V.; Agarwal, S. Influence of Surface Temperature on the Mechanism of Atomic Layer Deposition of Aluminum Oxide Using an Oxygen Plasma and Ozone. *Langmuir* **2011**, *28* (1), 350–357. https://doi.org/10.1021/LA201136K.

(72) Askeland, D. R. .; Fulay, P. P. .; Wright, W. J. *The Science and Engineering of Materials, 6th Edition*; Cengage Learning, 2010.

(73) Yamashita, T.; Hayes, P. Analysis of XPS Spectra of Fe2+ and Fe3+ Ions in Oxide Materials. *Appl. Surf. Sci.* **2008**, *254* (8), 2441–2449. https://doi.org/10.1016/j.apsusc.2007.09.063.

(74) Temperton, R. H.; Gibson, A.; O'Shea, J. N. In Situ XPS Analysis of the Atomic Layer Deposition of Aluminium Oxide on Titanium Dioxide. *Phys. Chem. Chem. Phys.* **2019**, *21* (3), 1393–1398. https://doi.org/10.1039/C8CP06912C.

(75) Lide, D. *CRC Handbook of Chemistry and Physics*, 88th Editi.; CRC Press Taylor & Francis: Boca Raton, Florida, 2007.

(76) Hämäläinen, J.; Ihanus, J.; Sajavaara, T.; Ritala, M.; Leskelä, M. Atomic Layer Deposition and Characterization of Aluminum Silicate Thin Films for Optical Applications. *J. Electrochem. Soc.* **2011**, *158* (2), P15–P21. https://doi.org/10.1149/1.3519497.

(77) Min, Y.-S.; Cho, Y. J.; Hwang, C. S. Amorphous High k Dielectric $Bi_{1-x-y}Ti_xSi_yO_z$ Thin Films by ALD. *Electrochem. Solid-State Lett.* **2004**, *7* (12), F85–F88.

https://doi.org/10.1149/1.1809558.

(78) Harjuoja, J.; Hatanpää, T.; Vehkamäki, M.; Väyrynen, S.; Putkonen, M.; Niinistö, L.; Ritala, M.; Leskelä, M.; Rauhala, E. New Approach to the ALD of Bismuth Silicates: $Bi(CH_2SiMe_3)_3$ Acting as a Precursor for Both Bismuth and Silicon. *Chem. Vap. Depos.* **2005**, *11* (8–9), 362–367. https://doi.org/10.1002/cvde.200506378.